GDCh Research Article Angewandte International Edition Chemie www.angewandte.org

How to cite: *Angew. Chem. Int. Ed.* **2026**, *65*, e20990
doi.org/10.1002/anie.202520990

Zinc Batteries

Regulating Solvent Co-Intercalation in Bi-Layered Vanadium Oxides for Zinc Batteries by Nanoconfinement Chemistry

Haocheng Guo, Mohsen Sotoudeh, Sri Rezeki, Yang Hu, Robert Leiter, Julia Wellmann, Maximilian Fichtner, Martin Oschatz, Axel Groß, and Simon Fleischmann**

Abstract: Electrochemical intercalation typically involves ion desolvation at the electrolyte–electrode interface, incurring kinetic limitations and strong ion-host interactions. The emerging mechanism of solvent co-intercalation, where ions intercalate together with a (partially) intact solvation shell, can mitigate these drawbacks, but has thus far been primarily explored from the viewpoint of electrolyte design. Herein, we demonstrate the feasibility of regulating solvent co-intercalation by electrode nanoconfinement design. Through the combined effects of decreasing interlayer water of bi-layered vanadium oxides and introducing molecules that tune the nanoconfining interlayer environment from hydrophilic to hydrophobic, the Zn^{2+} intercalation properties in aqueous electrolyte are modified. Comprehensive experiments and simulations reveal progressively reduced solvation/hydration of intercalating Zn^{2+} with decreasing interlayer hydrophilicity, affecting maximum capacity, redox potential, and kinetics of the electrochemical intercalation reactions. Similar electrochemical trends are observed in nonaqueous electrolytes, indicating the potential of nanoconfinement design as a universal strategy for regulating ion-solvent (co-)intercalation in various battery chemistries.

Introduction

Electrochemically-driven ion intercalation is the fundamental charge storage mechanism for many modern rechargeable batteries.[1–5] The intercalation reactions typically consist of three main steps: solvated ion migration through a liquid electrolyte to the electrolyte–electrode interface, interfacial charge transfer, and subsequent solid-state diffusion of the intercalant within the electrode host lattice.[6] For a typical charge transfer process, the coordinating solvent molecules of the liquid electrolyte are stripped off from the surface-adsorbed ions (i.e., desolvation), before the naked ion can then be inserted into the host lattice. From a simplified point of view, this step can be seen as a ligand exchange reaction as known from the field of inorganic coordination chemistry. Although the overall reaction is supported by entropy, the desolvation step is inevitably associated with an energy barrier presenting a kinetic limitation.[7]

An emerging strategy to overcome the disadvantages associated with desolvation is the intercalation of ions together with a (partially) intact solvation shell. This is also referred to as solvent co-intercalation.[6,8] Such reactions have gained momentum since the discovery of highly reversible co-intercalation of solvated Na^+ into graphite, a process that is thermodynamically prohibited for naked Na^+.[9] Co-intercalation phenomena are also encountered in other post-lithium energy storage like magnesium batteries,[10,11] and aqueous zinc- or proton-batteries.[12–14] Studies into the origins and the working mechanism are emerging.[15–17] Current strategies to regulate the feasibility and extent of solvent co-intercalation are, however, strongly focused on utilizing specialized electrolytes in both aqueous and organic systems.

[*] H. Guo, M. Sotoudeh, Y. Hu, R. Leiter, J. Wellmann, M. Fichtner, A. Groß, S. Fleischmann
Helmholtz Institute Ulm (HIU), Helmholtzstr. 11, Ulm 89081, Germany
E-mail: haocheng.guo@kit.edu
simon.fleischmann@kit.edu

H. Guo, M. Sotoudeh, Y. Hu, R. Leiter, J. Wellmann, S. Fleischmann
Karlsruhe Institute of Technology (KIT), Karlsruhe 76021, Germany

M. Sotoudeh, A. Groß
Institute of Theoretical Chemistry, Ulm University, Ulm 89081, Germany

S. Rezeki, M. Oschatz
Institute for Technical Chemistry and Environmental Chemistry, Friedrich-Schiller-University Jena, Philosophenweg 7a, Jena 07743, Germany

M. Fichtner
Institute of Nanotechnology (INT), Karlsruhe Institute of Technology (KIT), P.O. Box 3640, Karlsruhe 76021, Germany

M. Oschatz
Center for Energy and Environmental Chemistry, Friedrich-Schiller-University Jena, Philosophenweg 7a, Jena 07743, Germany

Additional supporting information can be found online in the Supporting Information section

The lack of consideration for regulating the co-intercalation properties of electrode materials presents a severe bottleneck, particularly for emerging multivalent battery chemistries where electrolytes are designed toward interfacial stability and whose electrolyte salts normally have low solubility, thus significantly reducing their tunability. Isolated reports of two-dimensional titanium carbide MXenes indicate that their surface chemistry can influence the extent of solvation of adsorbing or intercalating ions,[18,19] leading us to hypothesize that electrode design can be an alternative lever for tuning solvation. Consequently, there is an urgent need for exploring and understanding electrode materials design principles aimed at either promoting or inhibiting solvent co-intercalation, particularly regarding electrode materials commonly employed in state-of-the-art batteries, that is, layered transition metal oxides.

Pillaring approaches generally target the regulation of electrode materials' interlayer space, where intercalating species are hosted. They have been explored to modify the nanoconfining interlayer environment of host materials such as bi-layered vanadium oxides. However, these works mostly focus on the geometric aspect of nanoconfinement, for example, manipulating the interlayer spacing with spacer pillars of different dimensions,[20–23] neglecting the chemical environment of nanoconfined species. Capitalizing on the wide chemical diversity offered by organic molecules, we herein explore their capability as functional pillars to control the solvo-philicity of the host's interlayer environment and thus, introduce a paradigm-shift for regulating the extent of solvent co-intercalation as a function of nanoconfinement chemistry.

The proposed materials design principle is investigated using a series of bi-layered V_2O_5 hosts with modified nanoconfinement chemistries based on pillar molecules of varying hydrophilicity. Adopting established Zn^{2+} intercalation from aqueous electrolytes as a model reaction, comprehensive analyses disclose a clear trend of progressively reduced hydration of intercalating $Zn^{2+}(H_2O)_n$ upon decreased interlayer hydrophilicity of the host materials. The concept is also extended to organic electrolytes, confirming that the strategy of tuning nanoconfinement chemistry holds potential for diverse battery chemistries including those employing nonaqueous electrolytes.

Results and Discussion

Materials Synthesis and Characterization

A series of bi-layered V_2O_5 materials incorporating three different pillar molecules with varying polarity is synthesized by a bottom–up approach. Such variations in pillar functionality are hypothesized to affect the hydrophilic characteristics of the hosts' interlayer environments. These pillars are water (H_2O, the most hydrophilic inorganic pillar), 2,2′-(ethylenedioxy)bis(ethylamine) ($C_6H_{16}N_2O_2$, "EBEA", a hydrophilic organic pillar), and 1,8-diaminooctane ($C_8H_{20}N_2$, "DOA", a hydrophobic organic pillar). The choice is motivated by their varying lone electron-pair density, which is investigated through electron localization function (ELF) analysis. It is highest for H_2O, followed by EBEA, while DOA possesses the least accessible lone pairs (Figure 1a, Note S1). We hypothesize this as a general design principle to tune the hydrophilicity of the resulting nanoconfined interlayer environments of the host materials, which is validated by a combination of sorption experiments (Figure 1b). First, nitrogen sorption isotherms are analyzed. They indicate mostly macroporous samples with moderate specific surface areas (SSA) of around 25, 20, and 31 $m^2\ g^{-1}$ for V_2O_5–H_2O, V_2O_5–EBEA, and V_2O_5–DOA, respectively. These SSA values suggest the accessible external surface is similar across the samples. Pore size distribution profiles (Figure S1) further reveal predominant meso- and macropores for all samples with micropore volumes close to zero, indicating that the nanoconfining interlayer galleries (sub-nanometer scale, i.e., micropores) are not accessible to N_2 sorption experiments. Water vapor sorption isotherms show different trends. The sorption values far exceed the uptakes of N_2 at 100% humidity. V_2O_5–H_2O exhibits the highest sorption capacity up to 516 $cm^3\ g^{-1}$, followed by V_2O_5–EBEA (326 $cm^3\ g^{-1}$), and then V_2O_5–DOA (164 $cm^3\ g^{-1}$). Given that meso- and macro-pores are not determining water sorption, the large water uptake capacities suggest the involvement of the interlayer space.[24] Specifically, the high uptake of V_2O_5–H_2O at low humidity reveals a strong interaction with water and the presence of specific adsorption sites, suggesting an intrinsic tendency of xerogel(s) for spontaneous water intercalation/uptake (to be evidenced later). Moreover, the progressively reduced sorption volumes from H_2O to EBEA and to DOA pillared samples confirm the effectiveness of nanoconfinement manipulation in tuning solvo-philicity.

Electron microscopy characterization shows a nano-ribbon morphology of all samples (Figure S2 and S3). Powder X-ray diffraction (XRD, Figure 1c) results confirm lamellar ordering (though turbostratic) of all samples, as indicated by the prominent (*00l*) reflection(s) characteristic of bi-layered V_2O_5, in clear contrast to the α-V_2O_5 (Figure S4). The universal model (established from V_2O_5–H_2O)[25] depicts bilayers of single slabs for square pyramidal VO_5 units with water molecules (and other species) residing in between. However, determining the precise atomic structure of specific materials remains challenging. In practice, it is even common that existing powder diffraction file (PDF) patterns do not perfectly match synthesized materials, because these compounds are typically well-ordered in local range but lack long-range periodicity, with structural coherence limited to the nanometer scale. Consequently, only part of Bragg reflections can be detected in experiments, with their prominence affected by both synthetic and measurement conditions.[26] Varying interlayer species normally lead to changes in interlayer dimensions, manifesting as shifts in the (*00l*) reflections. Moreover, such modifications can induce rearrangements of associated atoms, possibly affecting other reflections. These collectively account for the observed differences across the materials. Overall, their (*001*) reflections appear at 2θ values of 6.39°, 7.28°, and 6.15°, corresponding to d-spacings of 13.82 Å (V_2O_5–H_2O), 12.13 Å (V_2O_5–EBEA), and 14.37 Å (V_2O_5–DOA), respectively. Moreover, differences in peak

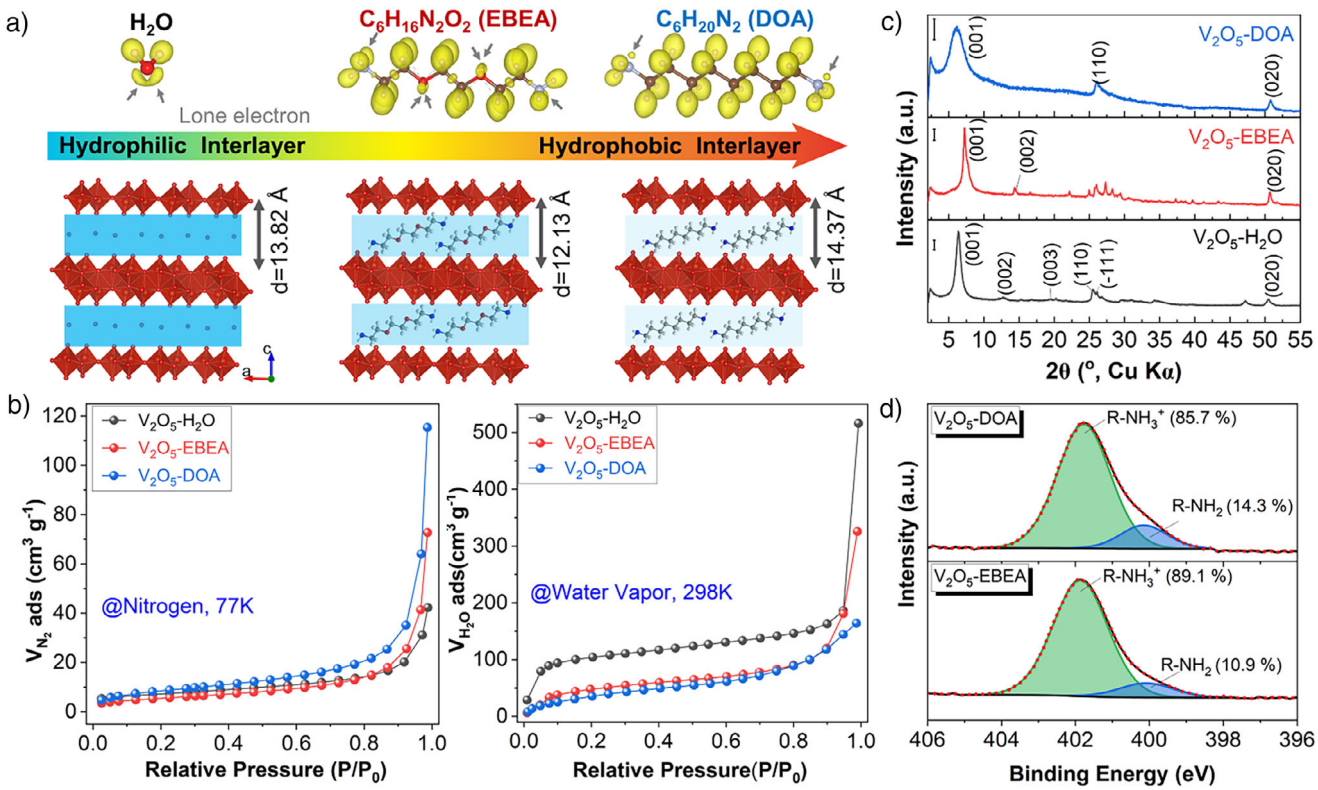

Figure 1. Physicochemical properties of the bi-layered vanadium oxide series. a) Electron localization function computed from first-principle simulation (iso-value of 0.7) and the correlated material modification strategy. A grey arrow indicates one lone electron-pair, and the progressively transparent blue blocks highlight the reducing hydration extents across the material series. b) Gas sorption isotherms of the materials, using nitrogen at 77 K (left) and water vapor at 298 K (right). c) Powder X-ray diffraction (XRD) patterns of the vanadium oxide series obtained in transmission geometry. The scale bars indicate the same intensity count. d) X-ray photoelectron spectroscopy (XPS) analysis of N 1s spectra for V_2O_5–DOA and V_2O_5–EBEA powders.

intensity and width indicate a decreasing trend of crystalline domain size, which is validated by microstructural analysis via transmission electron microscopy (Figure S3). Despite the slight variations in d-spacing and crystallite size, their extent was minimized and the influence on electrochemical performance was found negligible (as discussed later).

X-ray absorption spectroscopy (XAS, Figure S5) at the V K-edge reveals similar bulk chemical environments across the material series, closely resembling the reference α-V_2O_5 while exhibiting strong deviations from the centrosymmetric coordination. This aligns with the structure characteristics of bi-layered V_2O_5.[25] X-ray photoelectron spectroscopy (XPS) verifies consistent vanadium valence states across all materials (Figure S6), and further discloses the presence of ionic components from protonated alkylammonium pillars (Figure 1d).[23] This suggests ionic interaction between pillars and bi-layered vanadium oxides, where V_2O_5–H_2O is reported to confine hydroniums inside the interlayer.[27] Thermogravimetric analysis (Figure S7) quantifies the chemical compositions of the three samples as $V_2O_5{\cdot}1.168H_2O$ ("V_2O_5–H_2O", M_w = 202.92 g mol^{-1}), $(C_6H_{16}N_2O_2)_{0.271}V_2O_5{\cdot}0.362H_2O$ ("V_2O_5–EBEA", M_w = 228.57 g mol^{-1}), and $(C_8H_{20}N_2)_{0.259}V_2O_5{\cdot}0.184H_2O$ ("V_2O_5–DOA", M_w = 222.56 g mol^{-1}), respectively. Notably, crystal water can be detected in all samples, which is an intrinsic characteristic of bi-layered V_2O_5. This feature preserves partial hydrophilic nature of the V_2O_5–H_2O, contributing to the universal hydrated Zn^{2+} intercalation (as discussed later). Overall, both the more hydrophobic organic pillar molecules and the reduced crystal water contents synergistically modulate the interlayer hydrophobicity, as illustrated in Figure 1a. These combined effects make the chosen models well-suited for testing our hypothesis. Broadening the library of pillar molecules with different solvophilicity–solvophobicity balances could be beneficial for extended applications, while attention should be paid to the associated experimental limitations (Note S2).

Electrochemical Characterization

The electrochemical Zn^{2+} intercalation properties of the V_2O_5-based electrode materials series are tested as positive electrodes in a two-electrode setup (2032-type coin cells) versus zinc metal negative electrodes in aqueous electrolytes of 3 M zinc trifluoromethanesulfonate ($Zn(OTf)_2$). Zinc salts based on the OTf^- anion are chosen to minimize the potential influence from ion association (e.g., formation of ion pairs) in the electrolyte,[28] because lower cation–anion interactions

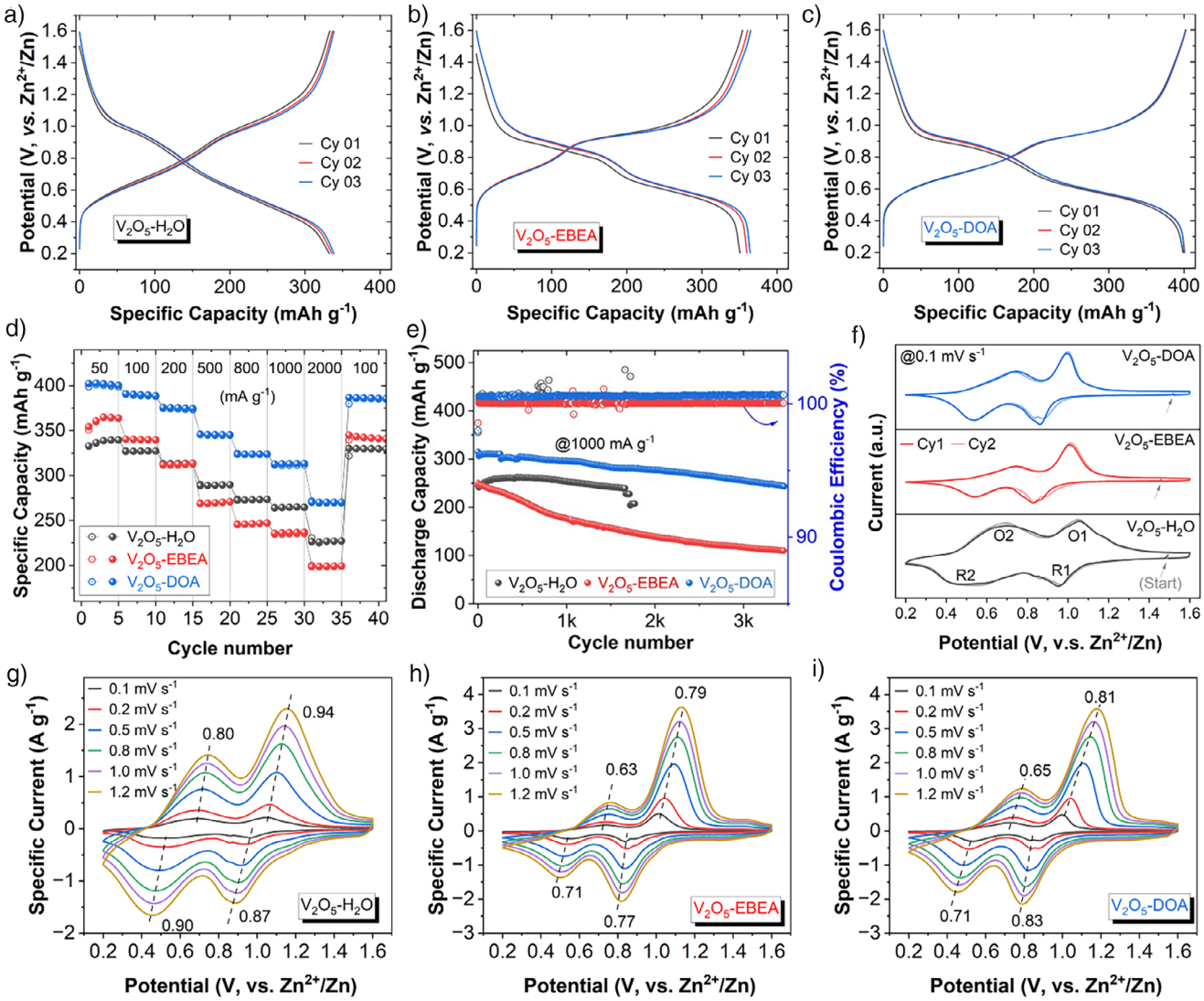

Figure 2. Electrochemical properties of the bi-layered V_2O_5 with varying interlayer chemistry in 3 M $Zn(OTf)_2$ electrolyte. Galvanostatic discharge–charge profiles of the initial three cycles for a) V_2O_5–H_2O, b) V_2O_5–EBEA, and c) V_2O_5–DOA at a specific current of 50 mA g^{-1}. d) Rate performance of the different electrode materials. Hollow and solid cycles correspond to discharge and charge processes, respectively. e) Long-term cycling performances of the materials series. Each cell was pre-cycled at 50 mA g^{-1} for 5 times before switching to 1 A g^{-1} current, and only the latter is shown for clarity. f) The initial CV profiles (Cycle 01–02) of the three materials at 0.1 mV s^{-1}. The starting potentials (labelled with grey arrows) were 1.52, 1.46, and 1.49 V for V_2O_5–H_2O, V_2O_5–EBEA, and V_2O_5–DOA, respectively. CV measurements of g) V_2O_5–H_2O, h) V_2O_5–EBEA, and i) V_2O_5–DOA electrodes at varying sweeping rates.

can be expected due to the reduced charge density with bulky anion size, facilitating Zn^{2+} dissociation. The highly hydrophobic nature of OTf^- helps to limit side reactions involving water molecules,[29] and also prevents a possible anion incorporation into the host's interlayer space. Furthermore, the electrolyte concentration was set as 3 M following previous reports,[12,30] to restrict the free solvent (water) activity and ensure the expected electrochemical performance. All samples exhibit highly symmetric and repeating discharge–charge profiles across the initial cycles, indicating little structural–chemical irreversibility in all three electrodes during the initial electrochemical reduction (Figure 2a–c). This is further underlined by the high initial Coulombic efficiencies (CEs), which are 99.90%, 99.11%, and 99.07 % for V_2O_5–H_2O, V_2O_5–EBEA, and V_2O_5–DOA, respectively (see also Table S1). Additionally, slight capacity increases are observed in their initial cycles, possibly due to an interface optimization of the V_2O_5 electrode leading to reduced impedances (Figure S8) and/or the zinc metal anode (with a native insulating oxide layer).

Tuning the nanoconfinement chemistry reveals a gradual capacity increase for decreasingly hydrophilic samples from H_2O- to EBEA- and DOA-pillared V_2O_5. Their cathodic capacities, normalized by the complete active material mass (V_2O_5 plus interlayer molecules), reach 339, 364, and 401 mAh g^{-1} at the 3rd cycle. To better understand these capacities with respect to the charge per transition metal, we also derive the corresponding electron transfer number per V_2O_5

as 2.57e$^-$ (V_2O_5–H_2O), 3.10e$^-$ (V_2O_5–EBEA) and 3.33e$^-$ (V_2O_5–DOA), respectively. This underlines the dependence of the capacity on the nanoconfinement chemistry. While concurrent H^+ intercalation across the whole potential range has been reported in vanadium oxides,[31] the contribution in our case is found to be limited (maximum protonation capacity is found in V_2O_5–H_2O, below ca. 40 mAh g^{-1}) in each sample when testing in dilute H_2SO_4 that matches the pH of 3 M $Zn(OTf)_2$ (Figure S9, Table S2, and Note S3). The potential influences from other structural parameters have also been excluded (Figure S10–S12 and Note S4). For instance, neither an enlarged d-spacing or a reduced crystallite size account for the higher capacity observed in V_2O_5–DOA, and V_2O_5–H_2O materials obtained by different synthesis exhibit comparable capacities and similar hydrophilic characteristics. Hence, the observed capacity differences across the materials can be primarily attributed to the tuned interlayer hydrophilicity and the consequently reduced solvation of the intercalating ions (to be demonstrated).

Rate handling measurements (Figure 2d) reveal that V_2O_5–H_2O surpasses V_2O_5–EBEA in capacity at higher specific currents, while V_2O_5–DOA maintains the highest capacity across all current densities. In addition to the tuned nanoconfinement chemistry, the superior capacity of V_2O_5–DOA at elevated currents can also be facilitated by the relatively smaller crystallite size and higher SSA. All samples show high CEs across various current densities, confirming the high chemical reversibility of the charge storage processes. Long-term cycling performances are compared in Figure 2e. The hydrophobic sample V_2O_5–DOA shows the best stability, with an overall capacity retention of 77% after 3450 cycles (approximately 85 days). In contrast, V_2O_5–EBEA experiences a fast capacity drop at the beginning, before gradually stabilizing (44% retention). V_2O_5–H_2O displays an initial capacity increase but rapid cell degradation after about 1600 cycles. Specific discharge–charge profiles and correlated dQ/dV plots (Figure S13) reveal consistent redox characteristics throughout cycling, indicating that the pillars of all samples are well retained within the bi-layered structures. Therefore, rather than pillar loss or structural degradation, the cycling performance of V_2O_5 is believed to be primarily restricted by the local pH fluctuations and the associated byproduct accumulation.[32] To exclude the influence of different rate capabilities and better reveal the intrinsic degradation behavior of V_2O_5, stability measurements were also conducted at a low current density of 100 mA g^{-1}(Figure S14). A decreased stability of V_2O_5–H_2O is detected, which can be mainly attributed to the growth of inactive zinc pyrovanadate caused by electrolyte pH changes.[32] This trend is supported by an increasing overpotential after 50 and 80 cycles visible from the potential profiles (Figure S14b). In comparison, V_2O_5–DOA still exhibits the most stable cycling performance over 27 days.

Differences in redox properties are further investigated in the cyclic voltammetry (CV) profiles (Figure 2f). Signals for V_2O_5–H_2O are generally characterized by two pairs of broad and symmetric peaks, where the low-potential pair appears more significant accounting for higher amount of charge storage. The redox signature of V_2O_5–EBEA and V_2O_5–DOA becomes sharper and less symmetric, accompanied with noticeable shifts in anodic/cathodic electrode potential compared to V_2O_5–H_2O. The first/high potential reduction (R1) peak of both V_2O_5–DOA and V_2O_5–EBEA samples shifts toward lower potentials compared to V_2O_5–H_2O. Notably, a slight peak split is observed across all samples at the first reduction zone, which merge together at increased sweeping rates. The high-potential redox peaks of the organically-pillared samples also become more pronounced, leading to increased capacities at elevated voltages. Contrarily, the second/low potential reduction (R2) peak of both V_2O_5–DOA and V_2O_5–EBEA samples shifts towards higher potentials compared to V_2O_5–H_2O. The shifts of redox peaks in different directions, as well as the significant change in CV shape between the samples are indicative of a variation in the intercalation mechanism. CV measurements at varying sweep rates were performed to analyzed the charge storage kinetics. With varying sweep rates (v), the response current (i) obeys a power–law function, $i = av^b$, where a and b are variable coefficients.[33] Figure 2g–i suggest a trend toward more surface-limited kinetics ($b = 1.0$) for V_2O_5–H_2O, whereas a mixed control and/or finite-length diffusion control ($b = 0.5$) is revealed for both V_2O_5–EBEA and V_2O_5–DOA samples. These observations align with the reduced solvation of intercalating ions.

Analysis of Solvent Co-Intercalation Behavior

Basic electrochemical characterization, discussed above, reveal differences in Zn^{2+} intercalation capacity, redox potentials, and kinetics among the different electrodes. We hypothesize that these differences arise from changes in the extent of solvent (water) co-intercalation, caused by the variations in nanoconfinement chemistry. Generally, solvent (water) molecules are expected to co-intercalate together with the ion (Zn^{2+}) into the host electrode only when accommodating the solvated ion lowers the free energy more than desolvation of the ion would cost. Since the desolvation energy within the aqueous 3 M $ZnOTf_2$ electrolyte remains the same across the materials, we hypothesize that the ability of the three different V_2O_5 hosts to stabilize the hydrated Zn^{2+} guests will determine the degree of (de-)hydration of the intercalating ions.

To verify, first, the electrochemical properties of the three electrode materials are evaluated in a non-aqueous electrolyte (Figure 3a–c) of saturated anhydrous $Zn(OTf)_2$ in acetonitrile (ACN), that is, in an environment where water co-intercalation can be ruled out. The solvating power of a solvent (ability to dissociate a salt) can be empirically correlated with its donor number (DN) and dielectric constant (ε).[34] In this context, ACN exhibits a weaker solvating power compared to water, as reflected by their respective DN (14.1 vs. 18.0) and ε (38.0 vs. 81.0).[35] Moreover, $Zn(OTf)_2$ shows substantially lower solubility in ACN (less than 1 M) than in water (~4 M[32]). Combining these theoretical parameters and experimental evidence, the resulting Zn^{2+} solvation complexes likely require reduced energy for desolvation,

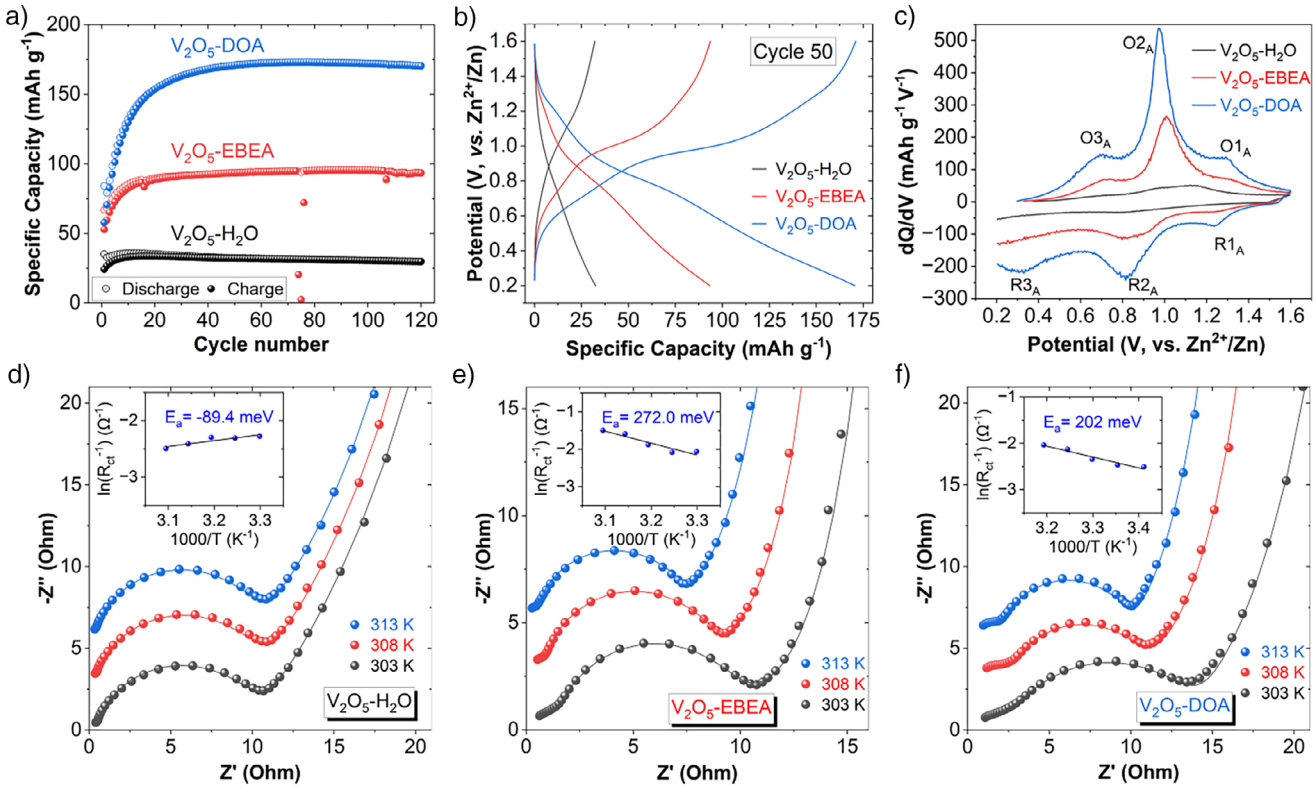

Figure 3. Validation of solvent co-intercalation in the V_2O_5 series. a)–c) Electrochemical properties of the various materials in a nonaqueous electrolyte ($Zn(OTf)_2$ in ACN). a) The cycling performances of the materials, b) their galvanostatic discharge–charge profiles at the 50th cycle and the corresponding c) differential capacity plots. d)–f) VT-EIS measurements for the material series in the aqueous electrolyte ($Zn(OTf)_2$ in water). The Nyquist plots for d) V_2O_5–H_2O, e) V_2O_5–EBEA, and f) V_2O_5–DOA under selected steps of varying temperatures. The insets show the Arrhenius plots of inverse R_{ct} values as a function of $1000/T$, with the slope values representing the activation energy for charge transfer.

thereby significantly decreasing the potential/extent of solvent co-intercalation.

This effect is reflected in a reduced capacity observed in the ACN-based electrolyte across all samples (Figure 3a,b) compared to the aqueous electrolyte. Furthermore, the ability of the materials series to enable nonhydrated Zn^{2+} intercalation can also be readily compared. Hydrophobic V_2O_5–DOA can host the highest number of nonhydrated Zn^{2+} (Figure 3b). This is followed by the intermediate sample V_2O_5–EBEA, while the most hydrophilic V_2O_5–H_2O sample shows very limited charge storage in non-aqueous electrolyte. This demonstrates the essential role of solvent (water) co-intercalation particularly in the hydrophilic V_2O_5–H_2O. Notably, redox profiles after 50 cycles (Figure 3c) reveal a distinct pair of redox peaks ($R2_A/O2_A$) in V_2O_5–DOA and V_2O_5–EBEA, which closely match the R1/O1 pair in aqueous electrolyte in both electrode potential and amplitude. In contrast, V_2O_5–H_2O exhibits severe polarization and negligible capacity. This is a strong indication that these redox signals correspond to the (de)intercalation of partially desolvated Zn^{2+} in both aqueous and nonaqueous electrolytes. (Noted, proton participation was ruled out in nonaqueous electrolytes.) Further electrochemical analysis can be found in Figure S15–S18 and Note S5. Moreover, it is worth noting that all samples exhibit highly consistent cycling performance in nonaqueous electrolytes where proton co-intercalation is excluded.

Back to aqueous electrolytes, the activation-controlled desolvation process during charge transfer is analyzed using varying temperature electrochemical impedance spectroscopy (VT-EIS)[36] in three-electrode cells. Nyquist plots exhibit a small (not obvious in V_2O_5–H_2O) and a large semicircle from high to medium frequency ranges, and then a sloping tail at low frequencies attributed to Warburg impedance that correlates to the mass transport in the bulk electrode lattice (Figure 3d–f). The intercept and semicircles correspond to solution resistance (R_s), a passivation layer resistance (R_p), and a charge transfer resistance (R_{ct}), respectively.[37] Upon temperature increase, V_2O_5–H_2O displays almost unchanged Nyquist profiles, with even slightly increased R_{ct} at further elevated temperatures (Figure S19). This indicates an activation-less charge transfer, where no physically meaningful activation barrier can be extracted from the Arrhenius plot. This finding aligns with the H_2O sorption capability of V_2O_5–H_2O (Figure 1b) and more generally the water-swellable nature of vanadium oxide xerogel,[38] thus providing again strong evidence for a desolvation-free water co-intercalation process in the hydrophilic sample. In sharp contrast, both V_2O_5–DOA and V_2O_5–EBEA are found to be associated with a typical temperature-dependent,

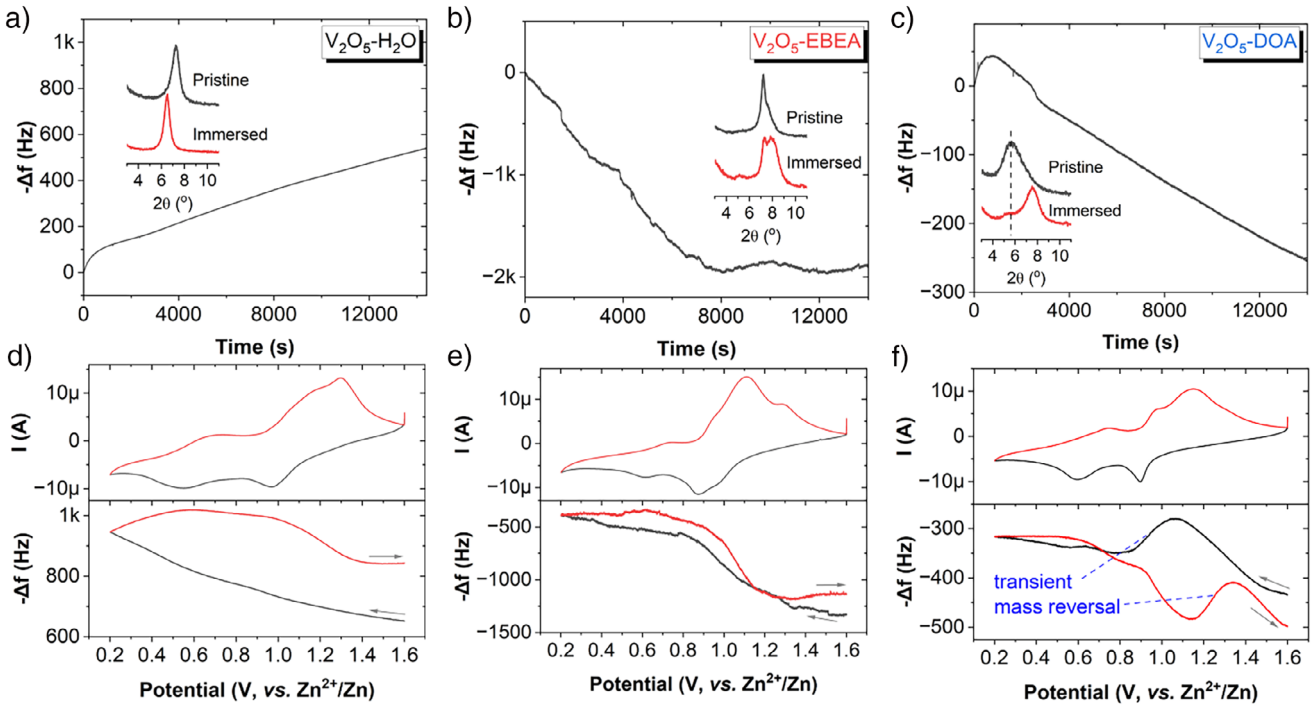

Figure 4. *Operando* observation of varying solvent co-intercalation. EQCM results for a), d) V_2O_5-H_2O, b), e) V_2O_5-EBEA, and c), f) V_2O_5-DOA in aqueous electrolytes. a)–c) Frequency evolution profiles (vs. time) during the OCP step, and the insets show normalized XRD results highlighting the corresponding electrode structure changes. d)–f) CV curves at 0.5 mV s^{-1} (2^{nd} cycle) with the corresponding frequency change profiles. For better understanding, the *Y*-axis has been plotted using negative frequency values, aligning with the mass change direction.

activation-controlled process, where an activation energy (E_a) is required to achieve charge transfer. This is evident from the noticeable shrinkage of the second semicircle (R_{ct}) with rising temperatures. These findings demonstrate that varying interlayer hydrophilicity (nanoconfinement chemistry) can effectively tune the desolvation-related charge transfer process, for example, energy barrier, resistance, and thus the extent of solvation of intercalating Zn^{2+}. Remarkably, the specific capacities for the materials follow the same order in both aqueous and nonaqueous electrolytes, implying a consistent trend in Zn^{2+} solvation. These results provide direct indications for broadening applicability of the proposed strategy to organic solvent systems. The expanded application can also be supported by our recent observations of organic solvents co-intercalation with Li^+ into V_2O_5 pillared by 1,12-diaminododecane.[23] Notably, while solvent co-intercalation in organic electrolytes may require a certain threshold of interlayer spacing, water co-intercalation is believed an intrinsic behavior in bi-layered V_2O_5 (Note S6).

This central finding is further verified via *operando* experiments using electrochemical quartz crystal microbalance (EQCM). Frequency changes were tracked for all materials starting from the resting period, as presented in Figure 4a–c using the negative values (comparison to the baseline signal of pure gold-coated quartz sensors given in Figure S20). Spontaneous water uptake is readily observed in V_2O_5–H_2O even prior to external electrochemical stimulation, by a decreasing frequency over time upon immersion in electrolytes. We qualitatively link this to mass gain of the electrode material according to the Sauerbrey equation,[39] as accurate gravimetric analysis requires rigid films [40] while nonelastic regimes are possibly encountered after electrode exposures to electrolytes. However, qualitatively, the results are well aligned with the water sorption isotherms (Figure 1b) and is accordingly attributed to free solvent (water) flooding into the V_2O_5–H_2O interlayer space.[17,41] This is further supported by XRD measurements (inset) where expanded d-spacing is detected. Interestingly, the opposite trend is observed in V_2O_5–DOA, with the electrode mass gradually decreasing. This can be mainly caused by partial desorption of confined species from the electrode, evidenced by the XRD detection of a new peak at reduced d-spacing. V_2O_5–EBEA shows similar initial mass decrease as V_2O_5–DOA but reaches equilibrium quickly after around 2 h. Notably, XRD results reveal more complicated structure changes with a minor reflection emerges at expanded d-spacing and the original (001) splits to generate another peak of lowered d-spacing. These suggest a dynamic mass exchange, possibly involving solvent uptake and confined species loss.

Figure 4d–f illustrate frequency evolutions of the electrode series during CV measurements in real time. V_2O_5–H_2O and V_2O_5–EBEA show monotonic evolution trends with frequency decrease (mass increase) during the intercalation step and frequency increase (mass decrease) during the de-intercalation process. Notably, V_2O_5–DOA shows a distinctly different evolution trend characterized by transient frequency (mass) reversals during both scans. Specifically, during

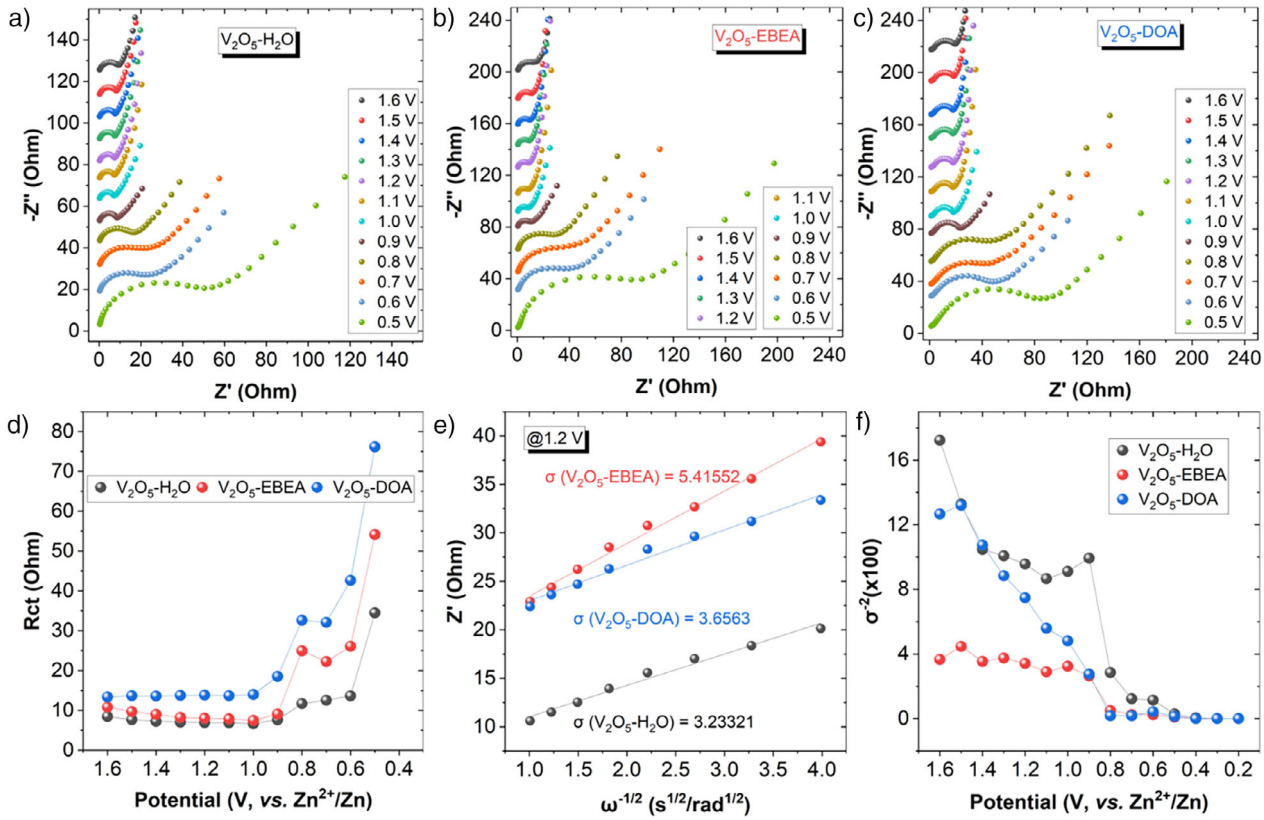

Figure 5. Dynamic impedance measurements during hydrated Zn^{2+} intercalation. Nyquist plots with y-axis offset of a) V_2O_5–H_2O, b) V_2O_5–EBEA, and c) V_2O_5–DOA electrodes at different states of charge, and the corresponding d) profiles of fitted R_{ct} values as a function of electrode potential across the material series. Interpretations of Warburg impedance, e) the Z' versus $\sigma^{-1/2}$ plots (@1.2 V vs. Zn^{2+}/Zn) for the three electrodes at low frequency regions. The slope of each fitted curve represents the Warburg factor (σ) for each specific electrode. f) The corresponding profiles of σ^{-2} as a function of electrode potential for three materials.

the cathodic scan (ion intercalation), the initial frequency decrease is followed by a frequency increase through the potential ranges for the 1st reduction peak (R1), after which the frequency decreasing trend resumes. Conversely, during the anodic scan, the increasing frequency trend reverses into a sharp frequency decrease approaching the peak potential of the major oxidation peak (O1), before eventually returning to an increasing trend at the end of the redox peak. This phenomenon is attributed to interfacial desorption (during intercalation) or adsorption (during de-intercalation) of solvent(-water), which reflects significant (de-)solvation processes around the major peak potentials (R1/O1).[13,42] These frequency change characteristics are highly reversible across multiple cycles (Figure S21). Overall, the findings strongly support our hypothesis of reduced hydration extent of intercalating Zn^{2+} into hydrophobic V_2O_5–DOA.

Influences of Nanoconfinement Chemistry on Zn^{2+} Intercalation

The fundamental properties of the intercalation processes are subsequently investigated from both kinetic and thermodynamic perspectives through impedance and structural analyses, respectively. Figure 5a–c display room temperature Nyquist plots obtained at varying (chronoamperometrically stabilized) states of charge during electrochemical reduction/discharge. All electrodes generally exhibit a similar evolution trend during the (co-)intercalation process. Their resistances (R_s and R_{ct}) stay mostly consistent above 0.8 V. Meanwhile the low frequency slopes (Warburg impedance) gradually decrease and notably reach ca. 45° at 0.9 V, indicating an increasingly diffusion-controlled electrochemical process. At 0.8 V, the semicircle associated with R_{ct} exhibits a significant increase and the Warburg slope remains at 45°. From 0.8 to 0.5 V, further changes are observed in R_{ct} with another notable increase at 0.5 V, while the Warburg slopes remain at 45°. The impedances rise significantly at the subsequent low potentials (Figure S22), indicating the end of intercalation procedure. Overall, substantial transitions in impedance have been identified at the same potential ranges, suggesting closely related structural evolutions to be discussed. There are also correlations between the varying interlayer hydrophilicities of host materials and their R_{ct} values.[6] In alignment with the highest hydration of intercalating Zn^{2+}, V_2O_5–H_2O displays the lowest R_{ct} value among the materials series, and their relative rank can largely maintain across the potential steps during the ion-intercalation process (Figure 5d).

Furthermore, dynamic changes of solid-state diffusion are also qualitatively analyzed via the impedance measurements.

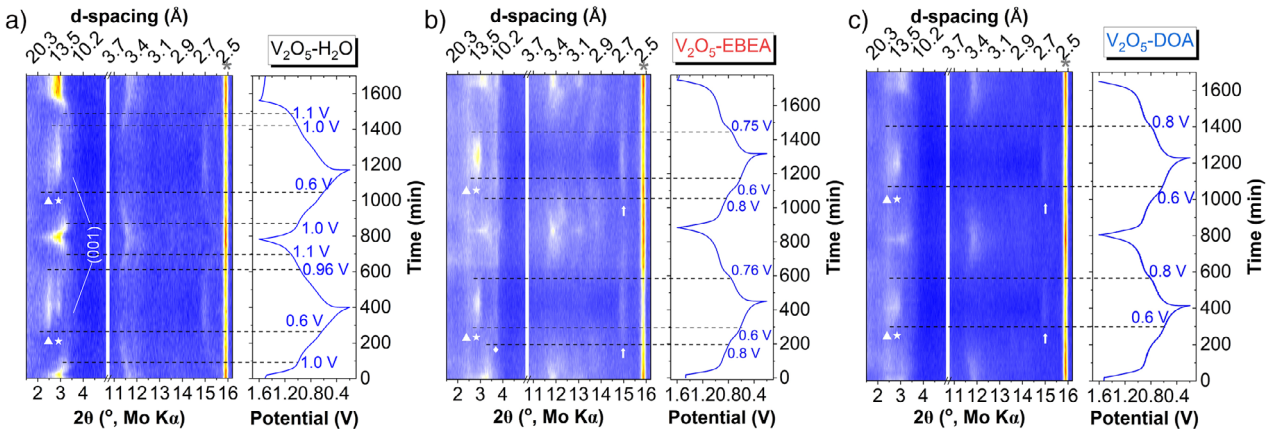

Figure 6. *Operando* structural analysis. XRD contour plots for a) V_2O_5–H_2O, b) V_2O_5–EBEA and c) V_2O_5–DOA electrodes. The "star" indicates the growth of basic zinc salts, and the "triangle" suggest the generation of an unknown structure. The arrow highlights the intensification/generation of a V–O coherent reflection which is absent in the pristine pattern.

This is achieved by Warburg factor (σ) of each spectrum according to Equation (1):

$$Z' = R_s + R_{ct} + \sigma\omega^{-1/2} \tag{1}$$

where ω designates frequency in *rad*. An example of the three electrodes at 1.2 V is displayed in Figure 5e. The V_2O_5–H_2O is seen with the minimal σ value similar to that of V_2O_5–DOA, while V_2O_5–EBEA shows a notable increase. This indicates an inverse trend for the efficiency of solid-state diffusion according to Equation (2):

$$D = \frac{R^2T^2}{2A^2n^4F^4c^2\sigma^2} \tag{2}$$

where D is the diffusion coefficient, R is the gas constant, T represents temperature, A is the area of electrode, n is the electron transfer number, F is Faraday's constant, c is the ion concentration inside lattice, and V_2O_5–H_2O is demonstrated with the most favorable diffusion characteristic. Due to the lack of precise c values, D could not be quantitatively calculated. Nevertheless, the changes in $1/\sigma^2$ obtained from the EIS measurements are further organized to qualitatively reflect the evolution of solid-state diffusion. As illustrated in Figure 5f, a clear ranking of diffusion characteristics can be identified, with V_2O_5–H_2O showing the highest values at most potential steps.

Structural evolution is subsequently investigated. Prior to electrochemical reactions, there are already sophisticated structure changes across all samples, as evidenced in EQCM and XRD results of soaked electrodes in electrolytes (Figures 4a-c and S23). Following dynamic changes during electrochemistry are tracked by *operando* XRD measurements (Figure 6). Two key regions of the diffraction patterns are highlighted, which correspond to the evolutions of the (001) plane and the most significant plane(s) associated with V–O coherence within the V_2O_5 bilayers, respectively. First, for all samples, it is identified periodic changes with repeatable diffraction features across two initial discharge–charge cycles (further cycles of V_2O_5–H_2O, see Figure S24), indicating high structural reversibility. These results align well with the discussed electrochemical observations (e.g., approximately 100% CE). Regarding the (001) reflection region, solid–solution changes and phase transition reactions can be tracked at similar potentials with ion (de)intercalation. These features match with the impedance measurements and suggest related reaction pathways within the material series. Among all samples, V_2O_5–H_2O shows characteristic solid–solution behaviors. During discharging, its (001) reflection shifts to higher angles (till ~1.0 V) with initial ion intercalation and then remains at a constant position but with intensity attenuation. Upon charging, the changes are well reversed, shifting back to original angles with increased intensities. However, the mentioned phase changes (e.g., 0.6 V in discharging) are found largely originating from byproduct formation(s), such as the growth of basic zinc salts (BZS, e.g., $Zn_{12}(OTF)_9(OH)_{15}$[30,31]) at roughly 2.92° (Mo Kα, consistent for the rest) and another unknown phase around 2.49°. The byproduct signals appear relatively strong and thus interfere the analysis of reflections from V_2O_5-EBEA/V_2O_5–DOA.

To minimize the interference, structure evolutions are further analyzed focusing on the V-O coherence reflections. In V_2O_5–H_2O, the original reflections both near 12° and before the substrate signals remain present throughout all electrochemical process though their intensity periodically attenuates or amplifies, and they display continuously minor position changes. These behaviors are characteristic of solid–solution reaction. Whereas in organic-pillared materials, signals of more intensive structure evolution can be detected, additional to the solid–solution changes: the peak near 12° becomes more attenuated upon higher degrees of Zn^{2+} intercalation, and this reflection almost disappears at 0.2 V; an additional phase-transition can be identified from the last displayed reflection, as the diffraction peak is absent (or too weak to detect) at the pristine state but notably emerge with ion intercalation and disappears during deintercalation. These findings indicate stronger ion-host-interactions in V_2O_5–EBEA/DOA, which likely originate from the intercalation of ions with lower hydration degrees.[43]

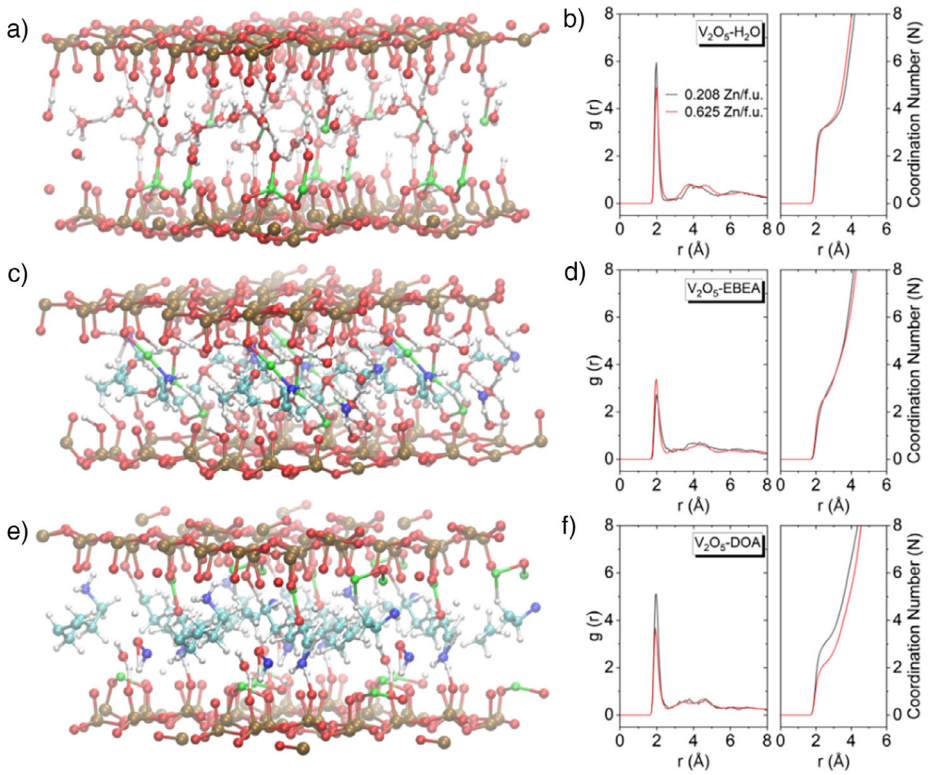

Figure 7. Ab initio molecular dynamics simulations. Simulated properties of a), b) V_2O_5–H_2O, c), d) V_2O_5–EBEA and e), f) V_2O_5–DOA, respectively. Side views of captured computation results for Zn^{2+} diffusion within a) V_2O_5–H_2O, c) V_2O_5–EBEA, and e) V_2O_5–DOA at a low ion loading. Zinc is shown in green, oxygen in red, vanadium in brown, hydrogen in white, nitrogen in blue, and carbon in cyan. b), d), f) Radial distribution function and the coordination number for the Zn–O pair of the electrode series.

Ex-situ XRD measurements verify these observations with improved resolution, although slight deviations are inevitable (Figure S25–S27). Overall, these structural results suggest 1) related reaction path of hydrated Zn^{2+} intercalation across the material series, accompanied with 2) progressively enhanced ion-host-interactions from V_2O_5-H_2O to organic-pillared V_2O_5, due to the intercalation of increasingly less hydrated ions. These findings are fully consistent with the discussed kinetic results obtained from impedance measurements (Figure 5) and *b*-value analysis (Figure 2g–i).

Atomistic Insights Into Ion Intercalation Processes

Ab initio molecular dynamics (AIMD) simulations are used to investigate the intercalation of Zn^{2+} ions into three types of V_2O_5-based materials, focusing on how the host lattice and confined molecules dynamically respond to electrochemical intercalation. The simulations focus on the initial solid–solution intercalation regime, which concludes following the first reduction peak (R1) in the CV curves.

Hydrophilic V_2O_5–H_2O (Figure 7a) shows strong hydrogen bonding within the interlayer space due to the high density of water molecules and lone pairs. These water molecules stabilize the framework and facilitate Zn^{2+} coordination with both water and lattice oxygens, forming two configurations. While Zn^{2+} typically exhibits six-fold coordination in aqueous electrolytes ($Zn(H_2O)_6^{2+}$),[44] simulations suggest rearranged coordination after Zn^{2+}–H_2O co-intercalation in the lattice, that is, Zn^{2+} does not remain as the fully solvated $Zn(H_2O)_6^{2+}$ complex upon intercalation. Radial distribution function (RDF) analysis (Figure 7b) confirms this, showing the first coordination shell of Zn–O around 2 Å with a reduced coordination number. At low Zn^{2+} concentration, no distortion of the V_2O_5 layer is observed, consistent with the structural measurements. This indicates minimal ion-host-interaction due to strong Zn^{2+} hydration.[43] At higher Zn^{2+} concentration, minor structural disruptions of the local Zn–O coordination appear, reflected by a drop in RDF intensity. These changes correlate with the subsequent phase transition observed in *operando* XRD upon further Zn^{2+} intercalation. Solid-state diffusion of Zn^{2+} occurs via both the confined water layer and in close proximity to the V_2O_5 layer, where the latter is analogous to surface-like diffusion with fast kinetics.[23] It should be noted that the hydration shell of intercalated Zn^{2+} within the V_2O_5–H_2O host can be composed of both water from the electrolyte and/or confined interlayer water.

In V_2O_5-EBEA, Zn^{2+} interact not only with water, but also with EBEA pillars, which contain oxygen atoms rich in lone pairs. They are part of the Zn^{2+}-coordination environment, as illustrated in Figure 7c. Therefore, Zn^{2+} intercalation leads to little structural distortion of the V_2O_5 lattice, but the Zn^{2+} transport is restricted to the confined EBEA layer, thereby limiting ion mobility and slowing electrochemical kinetics. RDF analysis (Figure 7d) show

weaker Zn–O coordination compared to V_2O_5–H_2O, but it becomes intensified at increased Zn^{2+} concentrations due to the interaction with EBEA molecules.

In the case of V_2O_5–DOA, Zn^{2+} predominantly coordinate with lattice oxygens, with no direct interaction with DOA molecules (Figure 7e). At low Zn^{2+} concentrations, ions reside close to the oxide layers rather than within the center of the interlayer. Despite the interaction with lattice oxygens, rapid Zn^{2+} mobility is observed through surface-like diffusion,[23] owing to few water molecules in vicinity (crystal water and/or co-intercalated water) which effectively serve as ligands. However, the stronger ion-host interaction leads to structural distortions of the oxide framework, which aligns with increased structural changes observed by *operando* XRD. The RDF profiles (Figure 7f) reveal a decline in Zn–O coordination with increasing Zn^{2+} concentration, indicating weakened lattice interaction. A drop of the coordination number at higher Zn^{2+} levels is observed only in V_2O_5–DOA, likely due to excess Zn^{2+} accumulating near DOA molecules but without forming bonds (Figure S28).

The RDF analysis on the V–O pair (Figure S29) verifies a similar distorted but well-defined coordination environments across all materials, where V_2O_5–DOA presents the most rigid V–O bonding network. AIMD and RDF analysis indicate that Zn^{2+} intercalation proceeds via partial desolvation: bulk $Zn(H_2O)_6^{2+}$ rearranges upon entering the interlayer, producing lower Zn–O coordination numbers than six (which remains dynamically changing) and host-dependent coordination motifs (water-rich in V_2O_5–H_2O, mixed H_2O and pillar-oxygen in V_2O_5–EBEA, and predominantly lattice-oxygen coordination in V_2O_5–DOA). The reduced Zn-O coordination number can be qualitatively validated by fitting X-ray absorption spectra on discharged electrodes (@0.2 V, Figure S30 and Table S3). However, contributions from additional phase(s) are evident, with V_2O_5–H_2O showing the highest value that probably corresponds to the most prominent secondary phase (Figure S25). The dynamic situation is further illustrated by Supplementary Movies 1–3. Overall, simulations reveal how the nanoconfinement chemistry critically affects Zn^{2+} coordination, mobility and intercalation-induced lattice distortion. These insights clarify the atomistic origins of the electrochemical behavior observed experimentally.

Conclusions

In this work, we demonstrate that solvent co-intercalation can be effectively regulated by electrode nanoconfinement design. A series of bi-layered vanadium oxides with tunable hydrophilicity of their interlayer space is synthesized to tailor the electrode–electrolyte interactions in an aqueous environment. Electrochemical Zn^{2+} intercalation from aqueous electrolytes shows strong dependence of the charge storage capacity, redox potentials and kinetics on the interlayer hydrophilicity. The most hydrophobic material, V_2O_5–DOA, exhibits improved Zn^{2+} storage capacity and stronger ion-host interaction. Using a range of *operando* characterizations and ab initio molecular dynamics modeling, a varying degree of solvent(water) co-intercalation has been identified as the origin for the observed differences in electrochemical performance. Moreover, hydrophobic V_2O_5–DOA also exhibits higher capacity in non-aqueous electrolytes than other samples, underlining its ability to accommodate anhydrous Zn^{2+} in varying electrolyte environments. These findings establish nanoconfinement chemistry as a powerful knob to tune solvent co-intercalation in layered transition metal oxide electrodes, opening new avenues to tailor electrochemical intercalation reactions and achieve novel batteries with efficient solvent co-intercalation.

Author Contributions

Haocheng Guo and Simon Fleischmann conceived and developed the study. Haocheng Guo performed materials synthesis, morphologic and thermogravimetric analysis, all diffraction and electrochemical experiments. Mohsen Sotoudeh conducted the computational study. Sri Rezeki and Martin Oschatz carried out the gas sorption measurements. Yang Hu performed the X-ray absorption spectroscopic measurements and analysis. Robert Leiter conducted the transmission electron microscopic measurements. Julia Wellmann performed X-ray photoelectron spectroscopic analysis. Maximilian Fichtner, Martin Oschatz, Axel Groß, and Simon Fleischmann supervised the work. All authors contributed to discussion of the results and writing of the manuscript.

Acknowledgements

H.G., R.L. and S.F. acknowledge funding from the German Federal Ministry of Research, Technology and Space (BMFTR) in the "NanoMatFutur" program (grant No. 03XP0423) and basic funding from the Helmholtz Association. J.W., M.F. and S.F. acknowledge funding from the German Research Foundation (DFG) through Project ID 390 874 152 (EXC 2154, POLiS Cluster of Excellence). H.G. is grateful for the support from Alexander von Humboldt foundation. The authors are grateful to Dr. M. Tobis (HIU) for guidance on EQCM analysis. The authors acknowledge SOLEIL Synchrotron for provision of beamtime (proposal no. 20240632) and Dr. S. Belin for assistance in accessing "ROCK" beamline. The beamtime work was supported by a public grant overseen by the French National Research Agency (ANR) as part of the "Investissements d'Avenir" program (reference: ANR-10-EQPX-45). Computer time provided by the state of Baden-Württemberg through bwHPC and the German Research Foundation (DFG) through grant no INST 40/575–1 FUGG (JUSTUS 2 cluster) is gratefully acknowledged.

Open access funding enabled and organized by Projekt DEAL.

Conflict of Interests

The authors declare no conflict of interest.

Data Availability Statement

Experimental data used in this work is made openly available on the Zenodo repository (https://zenodo.org) under the DOI: https://doi.org/10.5281/zenodo.17602559.

Keywords: Bi-layered V_2O_5 · Nanoconfinement chemistry · Solvent co-intercalation · Xerogel · Zinc-ion batteries

[1] R. Cui, Y. Ma, X. Gao, W. Wang, J. Wang, Z. Xing, Z. Ju, *Energy Stor. Mater.* **2024**, *71*, 103627, https://doi.org/10.1016/j.ensm.2024.103627.

[2] M. R. Palacin, P. Johansson, R. Dominko, B. Dlugatch, D. Aurbach, Z. Li, M. Fichtner, O. Lužanin, J. Bitenc, Z. Wei, *J. Phys. Energy* **2024**, *6*, 031501.

[3] Z. Li, S. Cui, J. Häcker, M. Nojabaee, M. Fichtner, G. Cui, Z. Zhao-Karger, *Angew. Chem. Int. Ed.* **2025**, *64*, e202415942.

[4] H. Guo, C. Zhao, *Small Methods* **2024**, *8*, e2300699.

[5] M. Shi, X. Zhang, *Adv. Mater.* **2025**, *37*, e2415676.

[6] H. C. Guo, M. Elmanzalawy, P. Sivakumar, S. Fleischmann, *Energy Environ. Sci.* **2024**, *17*, 2100.

[7] K. Xu, A. von Cresce, U. Lee, *Langmuir* **2010**, *26*, 11538–11543, https://doi.org/10.1021/la1009994.

[8] G. A. Ferrero, G. Åvall, K. Janßen, Y. Son, Y. Kravets, Y. Sun, P. Adelhelm, *Chem. Rev.* **2025**, *125*, 3401–3439.

[9] B. Jache, P. Adelhelm, *Angew. Chem. Int. Ed.* **2014**, *53*, 10169–10173, https://doi.org/10.1002/anie.201403734.

[10] Z. Li, X. Mu, Z. Zhao-Karger, T. Diemant, R. J. Behm, C. Kubel, M. Fichtner, *Nat. Commun.* **2018**, *9*, 5115.

[11] S. Hou, X. Ji, K. Gaskell, P.-f. Wang, L. Wang, J. Xu, R. Sun, O. Borodin, C. Wang, *Science* **2021**, *374*, 172.

[12] M. Yan, P. He, Y. Chen, S. Wang, Q. Wei, K. Zhao, X. Xu, Q. An, Y. Shuang, Y. Shao, K. T. Mueller, L. Mai, J. Liu, J. Yang, *Adv. Mater.* **2018**, *30*, 1703725, https://doi.org/10.1002/adma.201703725.

[13] H. Guo, S. Wu, W. Chen, Z. Su, Q. Wang, N. Sharma, C. Rong, S. Fleischmann, Z. Liu, C. Zhao, *Adv. Mater.* **2024**, *36*, e2307118, https://doi.org/10.1002/adma.202307118.

[14] H. C. Guo, S. Fleischmann, C. Zhao, *Nat. Sci. Rev.* **2025**, *12*, nwaf099, https://doi.org/10.1093/nsr/nwaf099.

[15] G. A. Ferrero, G. Åvall, K. A. Mazzio, Y. Son, K. Janßen, S. Risse, P. Adelhelm, *Adv. Energy Mater.* **2022**, *12*, 2202377.

[16] G. Åvall, G. A. Ferrero, K. A. Janßen, M. Exner, Y. Son, P. Adelhelm, *Adv. Energy Mater* **2023**, *13*, 2301944.

[17] Y. Sun, G. Avall, S. H. Wu, A. G. Ferrero, A. Freytag, P. B. Groszewicz, H. Wang, K. A. Mazzio, M. Bianchini, V. Baran, S. Risse, P. Adelhelm, *Nat. Mater.* **2025**, *24*, 1441–1449, https://doi.org/10.1038/s41563-025-02287-7.

[18] P. Barmann, R. Nolle, V. Siozios, M. Ruttert, O. Guillon, M. Winter, J. Gonzalez-Julian, T. Placke, *ACS Nano* **2021**, *15*, 3295.

[19] L. Liu, H. Zschiesche, M. Antonietti, B. Daffos, N. V. Tarakina, M. Gibilaro, P. Chamelot, L. Massot, B. Duployer, P.-L. Taberna, P. Simon, *Adv. Energy Mater.* **2023**, *13*, 2202709.

[20] K. Liang, R. A. Matsumoto, W. Zhao, N. C. Osti, I. Popov, B. P. Thapaliya, S. Fleischmann, S. Misra, K. Prenger, M. Tyagi, E. Mamontov, V. Augustyn, R. R. Unocic, A. P. Sokolov, S. Dai, P. T. Cummings, M. Naguib, *Adv. Funct. Mater.* **2021**, *31*, 2104007.

[21] Z. Xia, W. Chen, R. Shevate, Y. Wang, F. Gao, D. Wang, O. A. Kazi, A. U. Mane, S. S. Lee, J. W. Elam, S. B. Darling, *ACS Nano* **2022**, *16*, 18266.

[22] M. Elmanzalawy, H. Song, M. Tobis, R. Leiter, J. Choi, H. Moon, W. Y. Tsai, D. E. Jiang, S. Fleischmann, *Angew. Chem. Int. Ed.* **2025**, *64*, e202423593.

[23] J. Karol, C. O. Ogolla, M. Dillenz, M. Sotoudeh, E. Vollmer, M. Zarrabeitia, A. Groß, B. Butz, S. Fleischmann, *ACS Nano* **2025**, *19*, 26904–26919, https://doi.org/10.1021/acsnano.5c08169.

[24] P. Barboux, R. Morineau, J. Livage, *Solid State Ion* **1988**, *27*, 221–225, https://doi.org/10.1016/0167-2738(88)90213-5.

[25] V. Petkov, P. N. Trikalitis, E. S. Bozin, S. J. Billinge, T. Vogt, M. G. Kanatzidis, *J. Amer. Chem. Soc.* **2002**, *124*, 10157–10162, https://doi.org/10.1021/ja026143y.

[26] A. Moretti, S. Passerini, *Adv. Energy Mater* **2016**, *6*, 1600868, https://doi.org/10.1002/aenm.201600868.

[27] H. H. Kristoffersen, H. Metiu, *J. Phys. Chem. C* **2016**, *120*, 3986–3992, https://doi.org/10.1021/acs.jpcc.5b12418.

[28] M. R. Wright, *An Introduction to Aqueous Electrolyte Solutions*, John Wiley & Sons, New Jersey **2007**.

[29] W. Sun, F. Wang, B. Zhang, M. Zhang, V. Küpers, X. Ji, C. Theile, P. Bieker, K. Xu, C. Wang, *Science* **2021**, *371*, 46–51, https://doi.org/10.1126/science.abb9554.

[30] Y. Kim, Y. Park, M. Kim, J. Lee, K. J. Kim, J. W. Choi, *Nat. Commun.* **2022**, *13*, 2371, https://doi.org/10.1038/s41467-022-29987-x.

[31] X. Liu, H. Euchner, M. Zarrabeitia, X. Gao, G. A. Elia, A. Gross, S. Passerini, *ACS Energy Lett.* **2020**, *5*, 2979–2986, https://doi.org/10.1021/acsenergylett.0c01767.

[32] C. Lee, Y. Hong, D. Kim, Y. Lim, J. W. Choi, S. Y. Chung, *Adv. Funct. Mater.* **2023**, *33*, 2303763, https://doi.org/10.1002/adfm.202303763.

[33] S. Fleischmann, J. B. Mitchell, R. Wang, C. Zhan, D. E. Jiang, V. Presser, V. Augustyn, *Chem. Rev.* **2020**, *120*, 6738–6782, https://doi.org/10.1021/acs.chemrev.0c00170.

[34] J. Xu, J. Zhang, T. P. Pollard, Q. Li, S. Tan, S. Hou, H. Wan, F. Chen, H. He, E. Hu, K. Xu, X. Q. Yang, O. Borodin, C. Wang, *Nature* **2023**, *614*, 694–700, https://doi.org/10.1038/s41586-022-05627-8.

[35] V. Gutmann, *Coord. Chem. Rev.* **1976**, *18*, 225–255, https://doi.org/10.1016/S0010-8545(00)82045-7.

[36] Y. Mizuno, M. Okubo, E. Hosono, T. Kudo, H. Zhou, K. Ohishi, *J. Phys. Chem. C* **2013**, *117*, 10877–10882, https://doi.org/10.1021/jp311616s.

[37] S.-D. Han, S. Kim, D. Li, V. Petkov, H. D. Yoo, P. J. Phillips, H. Wang, J. J. Kim, K. L. More, B. Key, R. F. Klie, J. Cabana, V. R. Stamenkovic, T. T. Fister, N. M. Markovic, A. K. Burrell, S. Tepavcevic, J. T. Vaughey, *Chem. Mater.* **2017**, *29*, 4874.

[38] J. Livage, *Chem. Mater.* **1991**, *3*, 578–593, https://doi.org/10.1021/cm00016a006.

[39] G. Sauerbrey, *Z. Phys.* **1959**, *155*, 206–222, https://doi.org/10.1007/BF01337937.

[40] J. Miranda, P.-L. Taberna, P. Simon, *ACS Nano* **2025**, *19*, 2419–2426, https://doi.org/10.1021/acsnano.4c13052.

[41] X. Mu, D. Wang, F. Du, G. Chen, C. Wang, Y. Wei, Y. Gogotsi, Y. Gao, Y. Dall'Agnese, *Adv. Funct. Mater.* **2019**, *29*, 1902953.

[42] H. Guo, D. Goonetilleke, N. Sharma, W. Ren, Z. Su, A. Rawal, C. Zhao, *Cell Rep. Phys. Sci.* **2020**, *1*, 100225, https://doi.org/10.1016/j.xcrp.2020.100225.

[43] S. Fleischmann, Y. Zhang, X. Wang, P. T. Cummings, J. Wu, P. Simon, Y. Gogotsi, V. Presser, V. Augustyn, *Nat. Energy* **2022**, *7*, 222–228, https://doi.org/10.1038/s41560-022-00993-z.

[44] W. Xu, J. Li, X. Liao, L. Zhang, X. Zhang, C. Liu, K. Amine, K. Zhao, J. Lu, *J. Am. Chem. Soc.* **2023**, *145*, 22456.

Manuscript received: September 24, 2025
Revised manuscript received: October 28, 2025
Manuscript accepted: November 09, 2025
Version of record online: November 18, 2025